



Experimental and numerical studies of failure of a composite casing for a high-energy explosive

S. DeFisher^{1,2} · Y. W. Kwon¹

Received: 29 March 2024 / Accepted: 7 June 2024

This is a U.S. Government work and not under copyright protection in the US; foreign copyright protection may apply 2024

Abstract

Carbon fiber composite cylinders were fabricated using the filament winding technique, and the cylinders were loaded internally with a high-energy explosive material. As the high-energy explosive material detonated, the transient deformation and failure of the composite cylinder were investigated both experimentally and numerically. For the experimental study, a high-speed video camera running at 5 million frames per second was used to capture the deformation and failure of the composite cylinder. A Photonic Doppler Velocimetry (PDV) system was also used to measure the radial velocity of the outer wall of the cylinder while the internal detonation progressed. Separately, Split Hopkinson Pressure Bar (SHPB) tests were conducted to check the strain-rate effect on the failure strength of the carbon fiber material. Finally, a multiscale approach was used to model the dynamic deformation and failure of the composite cylinder. The multiscale technique considers the failure of composites in terms of the constituent materials like fiber and matrix materials. The numerically predicted deformation and failure agreed well with the experimentally observed and measured results.

Keywords Composite cylinder · High explosive · Failure · Multiscale technique · Photonic doppler velocimetry

1 Introduction

The use of polymer matrix and continuous fiber reinforced composites has grown as an alternative to more traditional engineering materials because of their beneficial properties such as high specific strength and stiffness as well as corrosion resistance. Engineering applications include pressure vessels and pipes with cylindrical geometries. As a result, polymeric fibrous composite cylinders were investigated both numerically and experimentally (Tennyson 1975; Roy and Tsai 1988; Noor et al. 1991; Hernández-Moreno et al. 2008; Hur et al. 2008; Blom et al. 2010; Siromani et al. 2014; Davies et al. 2016; Nelson and O'Toole 2018; Alaei et al. 2019; Kwon and Sugimoto 2020; Macapagal et al. 2024).

Composite pressure vessels are mostly subjected to static internal or external loading. However, they can also experience dynamic loading resulting from impact or explosion

(Nelson & O'Toole 2018, Alaei et al. 2019; Kwon and Sugimoto 2020; Macapagal et al. 2024). Another application of composite cylinders is a casing for high explosives. In this case, a high explosive was packed inside a composite cylinder, and detonated from one end of the composite cylinder. When tested in this manner, composite cylinders are subjected to very high strain-rate loading leading to complete failure. Even though metallic materials have been studied as a casing for high-energy explosives very extensively (Allison and Schriempf 1960; Tan et al. 2003; Du et al. 2021), far fewer studies have been conducted on explosively loaded fibrous composite cylinders (Beard and Palazotto 2006; Yao et al. 2009). Furthermore, few papers conducted both experimental and numerical studies simultaneously and compared the two results to the best of the author's knowledge.

Thus, the major task of the study was to investigate the transient, high strain rate, deformation, and failure of a carbon fiber composite cylindrical casing for a high explosive during detonation. Both experimental and numerical studies were undertaken, and their results were compared. The experimental study used Photonic Doppler Velocimetry (PDV) probes to measure the transient radial motion of the composite walls during the detonation process. The numerical study used a multiscale approach to determine

✉ Y. W. Kwon
ywkwon@nps.edu

¹ Department of Mechanical and Aerospace Engineering,
Naval Postgraduate School, Monterey, CA 93943, USA

² Picatinny Arsenal, Picatinny, NJ 07806, USA

the initiation of failure of the composite cylinder. Furthermore, Split Hopkins Pressure Bar (SHPB) tests were conducted to determine the effect of high strain rates on the failure strength of the carbon fibers that were used for the present study.

The mechanisms and modes of composite failure are complex, particularly for laminated fibrous composites. Many failure criteria have previously been proposed to predict failures in fibrous composites and are well summarized in the references (Sun et al. 1996; Hinton et al. 2002; Kadour et al. 2013). Most of the earliest composite failure theories applicable to modern polymer composites trace their inception back to the early to mid-1960s (Ashkenazi 1965; Gol'denblat and Kopnov 1965; Franklin 1968; Tsai and Pagano 1968). Later, more refined failure criteria were proposed by many research groups (Tsai and Wu 1971; Hashin and Rotem 1973; Hashin 1980; Puck and Schürmann 2004; Daniel 2007; Kwon and Darcy 2018a, b).

All the previous failure criteria are based on the strength of the lamina made of continuous fibers except for those in the references (Kwon and Darcy 2018a, b). The latter used a multiscale approach to determine the stress and strain at the fiber and matrix material level. Then, failure criteria were proposed at the fiber and matrix level. There are three potential failure modes at the constituent material level. They are fiber failure, matrix failure, and fiber-matrix interface failure. Interlaminar delamination is just one example of matrix and/or fiber-matrix interface failure. A failure criterion was proposed for each failure mode, resulting in a total of three failure criteria. The failure criteria at the constituent material level were used in this study and are described in greater detail later in this paper.

The primary objective of this study was to better understand and predict the failure of laminated fibrous composite cylindrical casings containing a high-energy explosive that was detonated from one side. To this end, both experimental and numerical studies were conducted one after the other, and their results were compared to each other.

The next section describes the preparation of Carbon Fiber Composite (CFC) cylinders for explosive testing which is followed by a detailed description of explosive testing and results. Then, numerical modeling and multiscale modeling are described. Later, numerical results and comparisons between experimental and numerical results are provided, followed by a summary and conclusions.

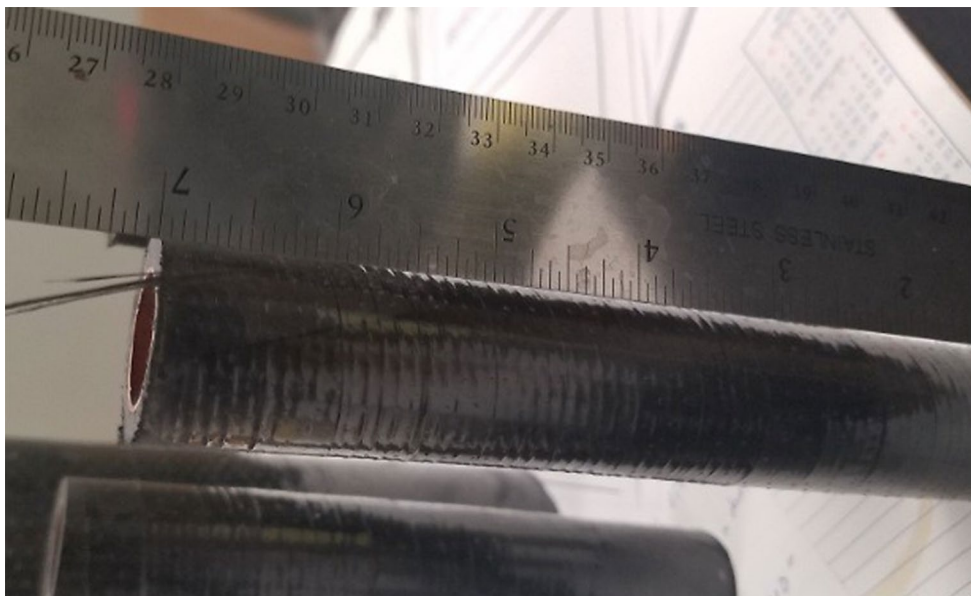
2 Preparation of composite cylinders for explosive testing

The testing samples were cylindrical, and they were fabricated using the filament winding technique using TCR™ Composites pre-impregnated tows comprised of a winding of Toray T700SC-50 C fibers with an embedded TCR's UF3325 resin. The composite cylinders of two different diameters were fabricated. One cylinder had an inner diameter of 2.26 cm and an outer diameter of 3.23 cm while the other had an inner diameter of 7.62 cm and an outer diameter of 8.59 cm. All the cylinders had the layer orientation of $(\pm 85^\circ, \pm 85^\circ \pm 45^\circ \pm 85^\circ, \pm 85^\circ \pm 45^\circ)$ where a 90° winding is strictly circumferential and a 0° winding is strictly longitudinal. It should be noted that the filament winding machine lays down the $+85^\circ$ layer while traveling down the mandrel axis in one direction and then lays the -85° while traveling in the opposite direction. This type of orientation resembles a twill or fabric with a seam of layers running in opposite directions rather than a single $+85^\circ$ layer that forms a complete layer of itself with a -85° layer on top of it.

After completion of the winding, the fiber wound mandrel was wrapped using shrink tape and then placed in an oven for curing. This curing process causes the tape to shrink and forces the epoxy, already pre-impregnated into the fiber tow of which the structure is comprised, to flow within the confines of the tape and mandrel such that the finished product is a uniform composite structure identical to that which would have resulted had a dry fiber been pulled through a resin bath and cured using more conventional vacuum bagging technology. The finished sample was then removed from the mandrel, most often by pressing it out. The filament wound cylinders were cut using a band saw. Figure 1 shows a final composite cylinder of a smaller diameter. The lengths of the small and larger diameter cylinders were 17.8 cm and 7.62 cm, respectively.

The carbon fibers had the elastic moduli of $E_L = 225$ GPa and $E_T = 15$ GPa where the subscripts L and T denote the longitudinal and transverse directions, respectively. Their shear moduli were $G_{LT} = 0.2$ GPa and $G_{TT} = 7$ GPa. The Poisson's ratio was $\nu_{LT} = 0.2$, the tensile strength was 4.9 GPa, and the mass density was 1.8 g/cm³. The matrix had an elastic modulus of 2.8 GPa, Poisson's ratio of 0.35, mass density of 1.21 g/cm³, and tensile strength of 79 MPa. The fiber volume fraction is 0.5. Both fiber and matrix materials were assumed to be linear elastic until failure. In addition, because the whole process was so quick, it was considered that there was not enough time for heat transfer. As a result, no thermal analysis was conducted.

Fig. 1 Filament wound CFC cylinder



3 Explosive testing and results

The CFC samples were hand-loaded with a moldable explosive after which they were permanently mounted into a fixture designed to hold the PDV probes. An example of an early fixture designed to hold the larger CFC cylinder with an aluminum buffer can be seen in Fig. 2. It is important to note that the test setup was the same for all the tests regardless of the aluminum buffer inside the composite cylinders.

All samples were secured into the fixture using epoxy to ensure stability and orthogonality between the test article and the laser emitted from the PDV probe. Although reflectivity was initially a concern, it turned out not to be an issue and the data could be gathered without the need to enhance surface reflectivity.

Initial tests were conducted without using any PDV probes. A few different types of strain gauges were used to gather strain data. These included both traditional Omega SGD-7/350- LY11 gauges in addition to Dynasen Mn/Cn4-50-Ek gauges. All gauges were bonded to the outer surface of the CFC samples using an M-bond AE-10 strain gauge adhesive. All these tests were conducted using the explosive composition C4 due to its availability and ease of use which allowed the test articles to be consistently and uniformly loaded. The C4 was loaded piecemeal using a wooden dowel to ensure that no air gaps or imperfections existed because air gaps could have changed the test results had they been of sufficient size or numbers. Using a malleable explosive had the added benefit of conforming to any surface imperfections alleviating concerns of asymmetric expansion or irregular velocity that could have resulted from defects created during the manufacturing process. The characteristics of the explosive used for subsequent modeling are shown

in Table 1. These are commonly referred to as the Jones-Wilkins-Lee (JWL) Equation of State (EOS) parameters (Lee et al. 1973). The equation is provided below:

$$p = A \left(1 - \frac{\omega}{R_1 V} \right) e^{-R_1 V} + B \left(1 - \frac{\omega}{R_2 V} \right) e^{-R_2 V} + \omega \frac{W}{V} \quad (1)$$

where p is pressure, W is energy, and V is the relative specific volume that is equal to v/v_0 . Here v is the present volume, and v_0 is the specific volume which is the inverse value of the initial density of the explosive.

The detonators used for all tests were RISI RP-502 economy exploding bridge wires (EBW). These detonators, essentially the equivalent of a #8 blasting cap with respect to explosive output, are commonly used in testing due to their inherent safety requiring a minimum of 500 V to initiate. Although not as precise as other members of the EBW family, they cost much less yet still initiate with a standard deviation of less than 500 ns. This was more than sufficient for the timing of the magnitude that was expected here.

Although the various strain gauges should not have had any limitations with respect to acquiring data at the rates generated by explosive loading, they were susceptible to high frequency transient noise even when shielded to the fullest extent possible. Shortening the leads and dropping the voltage to a minimal level to fire still did not alleviate the problems with noise. Although the detonation wave should have reached the plane of the strain gauge at about 4.7 μ s owing to the variability in the detonator, the transit times of the signals involved, the scope reading the signal, and possibly other factors; a small amount of variation could not be overcome. Figure 3 shows the raw strain gauge output, i.e. voltage as a function of time, for two tests. The

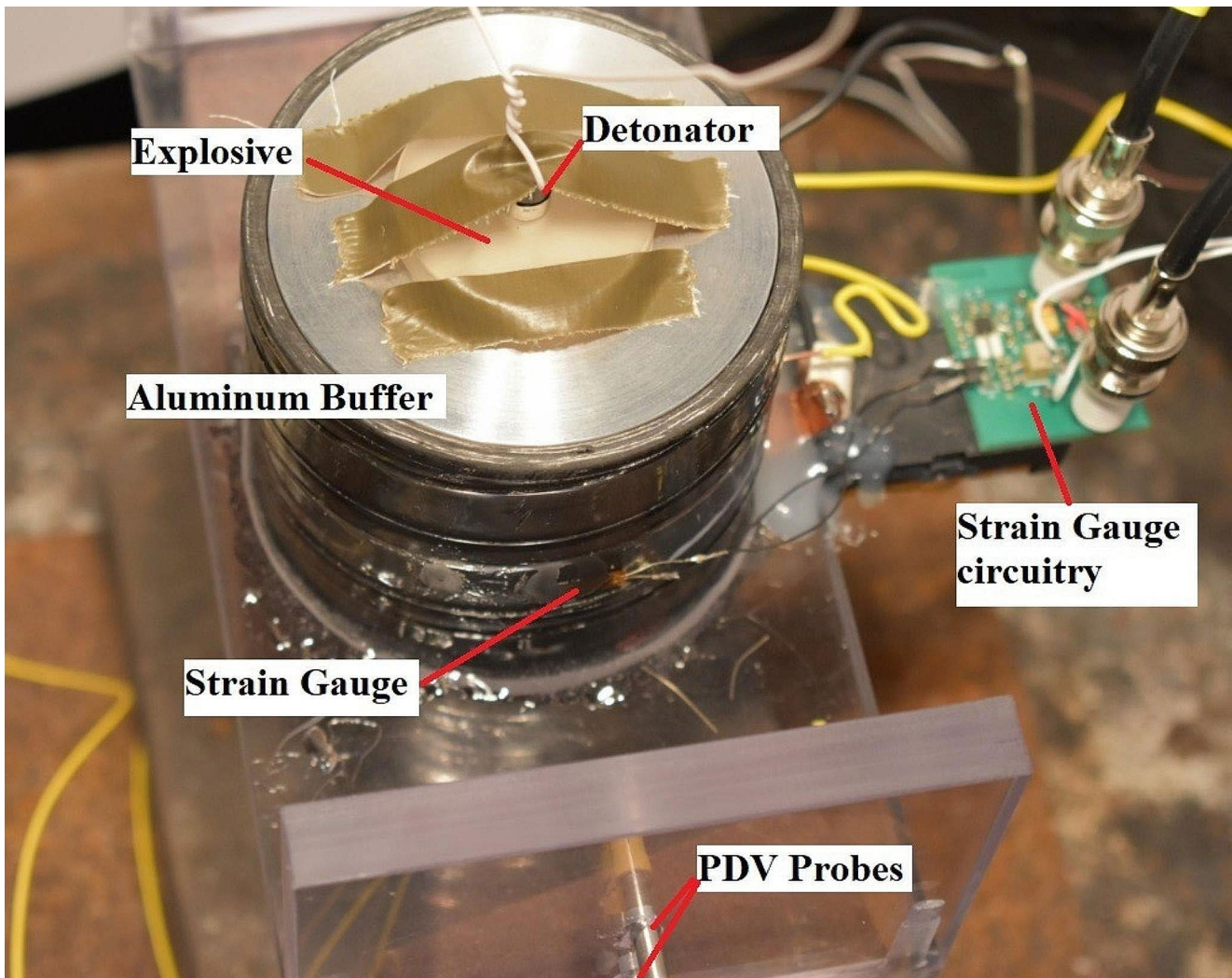


Fig. 2 Large CFC cylinder experimental setup

Table 1 Composition C4 JWL Parameters

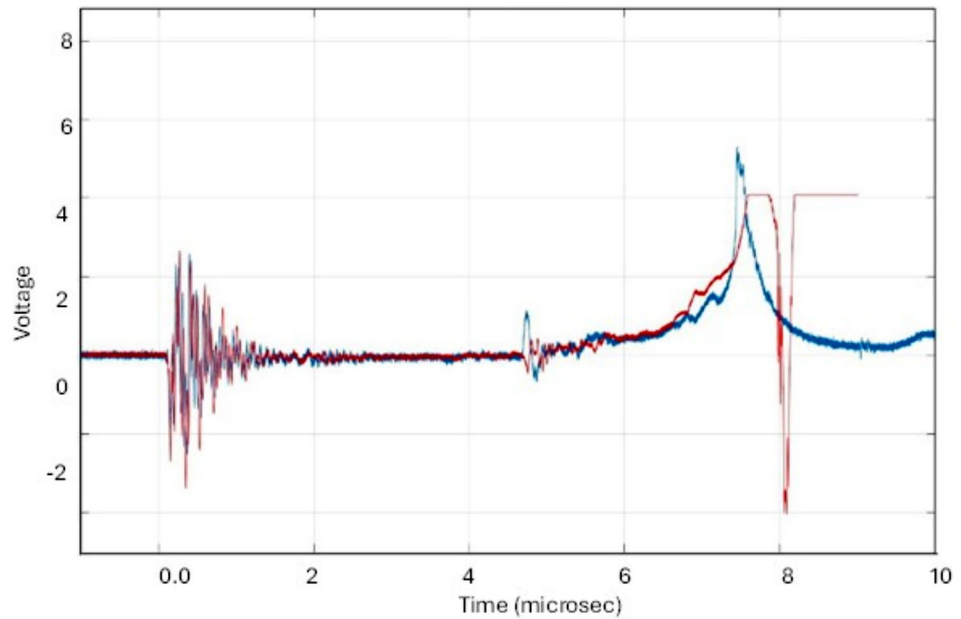
ρ (g/cm^3)	Det velocity ($cm/\mu s$)	A (Mbar)	B (Mbar)	R_1	R_2	ω
1.601	0.8193	6.833	0.148	4.7	1.5	0.28

first signals at roughly $0.2 \mu s$ were noise induced by the firing pulse going to the detonator. The pulse that occurs at a little under $5 \mu s$ was believed to be the initial reading of the strain gauge albeit with unexpected oscillatory behavior. An early hypothesis for why this oscillation occurred was due to a rapid reflection of the incident shock from the outer CFC surface. This hypothesis was quickly abandoned, however, because it was believed to be highly unlikely that the spall strength of the adhesive used to affix the gauge would have been sufficient to hold the gauge onto the cylindrical surface after the initial incident shock. This signal was therefore hypothesized to be some type of noise coupling to the strain gauge output with the actual reading occurring somewhere in the rising voltage almost immediately after

that point. Unfortunately, although the trend of the signal was as expected, namely increasing to some failure strain, it still suffered from an extremely high signal-to-noise (S/N) ratio making it very difficult to determine exactly when the readings began and ultimately where failure had occurred.

The high frequency transient noise on the strain gauge channel is believed to have been the result of at least two separate events. The first high frequency decaying signal that can be seen in Fig. 3, is believed to be due to the EBW. Because EBWs require such a high initiation voltage, and by the nature of the location of the detonator to the strain gauge that was mounted to the outside of the CFC cylinder; the magnetic pulse that naturally occurs as a result of the EBW was believed to couple to the strain gauge contributing

Fig. 3 Strain gauge voltage vs. time (2 large CFC samples)



to the noise seen here. Although magnetic shielding of the strain gauge lines was attempted, in addition to dropping the voltage to the minimal level to consistently initiate the detonator; all attempts to diminish this noise were unsuccessful.

In addition to the electrical and magnetic noise from the high voltage pulse sent to the detonator, the extremely rapid exothermic transformation from condensed phase explosive comprised of C, H, N, and O atoms into intermediate molecules including CO, CO₂, H₂O, N₂, NO_x, and other products, generates a conductive soup of rapidly changing chemical species. A rapidly evolving cloud of dissociated ions and conductive chemical species develops on the order of microseconds within a region of increasing pressure, temperature, and dynamic chemical species. It only took about 22 μs to consume all the solid explosives used here. Some researchers have demonstrated that polymers tend to experience changes in electrical conductivity and polarization as a result of experiencing a strong shock (Dattelbaum and Coe 2016). Depending on the polymer, these changes may occur between 20 and 30 GPa. The detonation pressure, for composition C4, is slightly over 27 GPa which places it solidly within the range of likely experiencing changes of conductivity for at least a portion of the matrix of which the CFC cylinder is comprised.

If a shock of this magnitude occurs, then the chemical dissociation of a shocked polymer is likely yet another contributing factor to the high frequency transient noise that made it impossible to consistently collect clean output from the strain gauges. As a result of this inability to extract useful strain gauge data, in addition to the inability to precisely synchronize strain gauge measurement with the beginning of the event, i.e. usually the firing signal to the detonator;

strain gauges were abandoned in favor of the optical technique known as PDV. This technique provided a direct optical measurement of velocity and as a result, was free from problems associated with excessive radio frequency noise introduced by high voltage and the need to measure extremely rapid and sensitive electrical signals using nearby gauges.

The PDV is a technique developed by O.T. Strand at Lawrence Livermore National Laboratories (Strand et al. 2005; Mercier et al. 2006; Dolan 2020). It is a relatively new technique and is now widely used. The technique is based on other interferometric techniques that have been used since the late 1960s. This simpler and more modern method uses laser light split in two distinct streams where one is focused on a reflective surface of interest and the other is used as a reference. When the surface of interest moves rapidly as in the case of a detonation; the reflected laser light, i.e., the light that has been doppler shifted, and the unshifted reference light are collected by a detector. The combination of these two distinct light waves causes a beat phenomenon wherein after they are added they interfere with each other. This interference results in a waveform with a distinct pattern or beat frequency that is proportional to the velocity of the measured surface. This technique also allows for extremely accurate measurement of velocity at a much lower cost and complexity than the previous types of diagnostics used for similar measurements. This technique has largely replaced older, larger, and more complicated interferometric systems including the Velocity Interferometer System for Any Reflector (VISAR) and the Fabry-Perot interferometer.

When we switched from using strain gauges to using PDV probes, we simultaneously transitioned to a longer sample with a smaller diameter. This new aspect ratio sample had an inner diameter measuring 2.26 cm and an outer diameter of 3.23 cm as shown in Fig. 1. These were loaded by hand with composition C4 and placed into a fixture that allowed the mounting of facing PDV probes as shown in Fig. 4. The PDV probe locations were chosen such that two pairs were located collinearly opposite each other measuring velocity on opposite walls of the test article. The first pair of the PDV probes was located at 6.6 cm from the outer surface of the tube and at 7.62 cm down from the detonator. The second pair was located another 6.08 cm down from the first pair. This was done to ensure that the detonation would be fully evolved and had reached a steady state.

The CFC cylinder was loaded with C4 and glued into the fixture after which the top plate was bolted down, and the PDV probes permanently attached to the sides. Because we did not have a consistent and predictable angle at which the cylinder would diverge from the vertical wall as detonation was initiated from the top, it was impossible to guess at a more accurate angle to align the probes in a perpendicular sense so they were mounted perfectly perpendicular to the outer wall of the CFC cylinder by boring blind holes into the supporting PMMA sides. This is important to remember when we analyze the data for this test in the following section.

As we wished to gather optical data on the progression of detonation in addition to wall velocity from the PDV probes, a white backdrop of cardboard was used to reflect light. A Kirana 5 M camera was used with a framing rate of 5 million frames per second. At such a high framing

rate, additional light is necessary to illuminate the event of interest. The additional light was generated using 3 pairs of xenon flash bulbs (not shown in Fig. 4) triggered in series from the detonator, with different delays, to illuminate the event over the duration of time that the camera could capture frames. Several of the still images can be seen in Fig. 5.

These images were captured at approximately 15, 17, and 21 μs respectively, which showed representative behaviors of the composite cylinder during its deformation and failure process. Although the camera was triggered by the signal running to the detonator, it was difficult to precisely synchronize it with the event owing to the fact that the line lengths were somewhat different and the xenon flashbulbs used for illumination did not instantaneously produce usable light. It took time not only for the signal to reach the xenon flashbulbs but also for them to begin producing light. Evidence of the imprecise illumination timing is that many of the earliest frames were black. These lights, set up in 3 banks of 2 were staggered to come on at different times during the event. Because of that, in addition to the variable duration over which they produced visible light, they exhibited a breathing-like behavior where the light alternated between becoming brighter and darker before eventually being consumed completely. Nonetheless, most of the event, except for very early times, was captured. The later images suffer from overexposure resulting from the break-out of gaseous detonation products from the wall which has reached several volume expansions and appears to have already failed in numerous locations. If we enlarge one of the earlier frames, however, we can see some interesting behavior. Figure 6 is a larger version of the leftmost image above.

Fig. 4 Small diameter CFC experimental setup with PDV probes

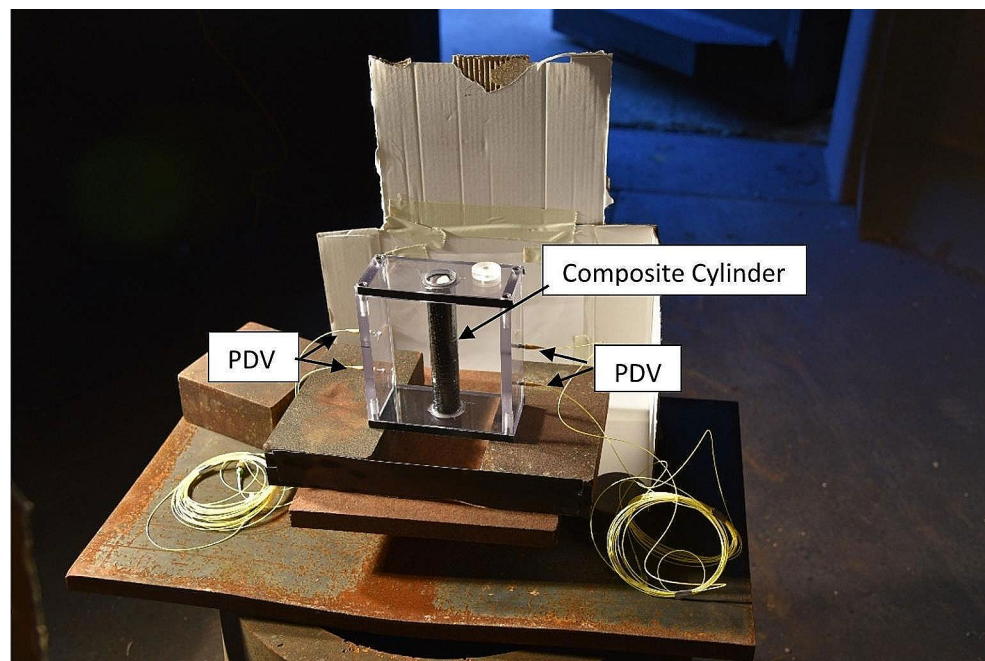




Fig. 5 Three high-speed video frames of explosively driven CFC at 15, 17, and 21 μ s

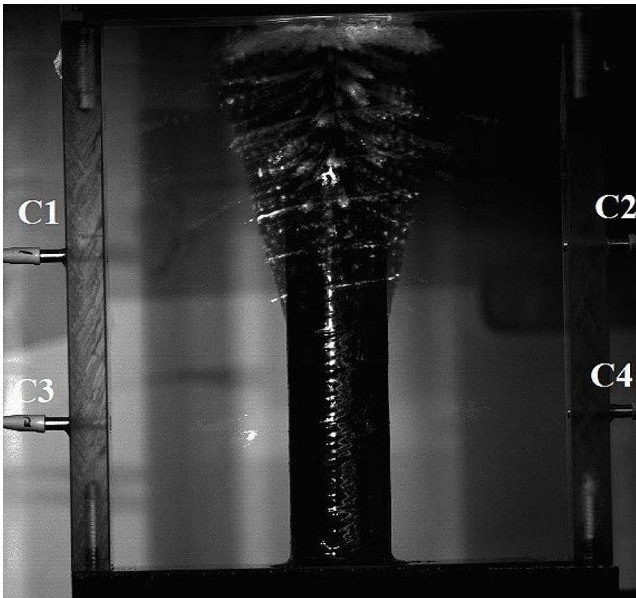


Fig. 6 CFC cylinder approximately 15 μ s after initiation

Several important things can be seen within this frame. The first is that the gaseous products appear to have forced their way through the various layers in several locations. Evidence of this is the consistently lit rings that are shown in the expanding region of the CFC tube. What is noteworthy about that fact is that they appear to be the angles closest to circumferential in the ($\pm 85^\circ \pm 85^\circ \pm 45^\circ \pm 85^\circ \pm 85^\circ \pm 45^\circ$) layup of the composite cylinder. Being able to see light through any of the 85° layers means that the preceding layers had to have already failed at least to some degree. In addition, from closer examination of the photograph it appears as if at least the outer layer of polymer in the matrix has spalled because of exposure to a high shock pressure. The phenomenon of spall occurs when an incident shock reflects from a free surface as a tensile wave and interacts with its rarefaction. When that occurs, the material is placed in tension. If the magnitude of that tension is larger than the

tensile strength of the material, it fails. In this scenario, the spall is radially distributed and results in a field of ejected polymer. In the case of an ordinary metal such as the copper used in a conventional cylindrical expansion experiment (CYLEX), this material remains solid until failure occurs, but the polymer is unable to bear that load similarly. What is seen and measured for this explosively loaded CFC tube is a radially expanding debris field comprised of spalled polymer from the matrix, preceding an expanding layer of fibers from which it has separated at least to some degree instead of an intact, monolithic, radially expanding wall,

Evidence of this being a field of spalled matrix is supported by the fact that in the optical photograph of Fig. 6 where you can see lines of light shining through at a consistent $\pm 85^\circ$ angle from the positive downward direction. This light is only visible in the region of the CFC tube that has expanded radially outward to even a slight degree. Although not conclusively an indication of anything other than ordinary failure, examination of the raw PDV data provides another clue as to the nature of this failure. PDV gauges are only able to read a sufficiently reflective surface. Therefore, if at any time such a surface did not exist or was becoming less reflective in time, this would be an additional indication that gaseous products had leaked from the expanding cylinder indicating that failure had already occurred. A consequence of this is that sometime after spall occurs, any PDV probe data will rapidly become untrustworthy as it will be too broken and intermingled with high velocity, high pressure, and high temperature gases that have pushed their way through the various layers to be measuring the wall or even its remnants. This was seen in the reduced PDV data as shown in Fig. 7.

When the raw PDV data of the CFC cylinder is compared with the raw data for a similar test conducted on a steel cylinder, the CFC data has a few distinct differences. The most important difference is that the steel PDV data contains a long duration signal that is clear and consistent. This type of signal is indicative of a reflective surface that although

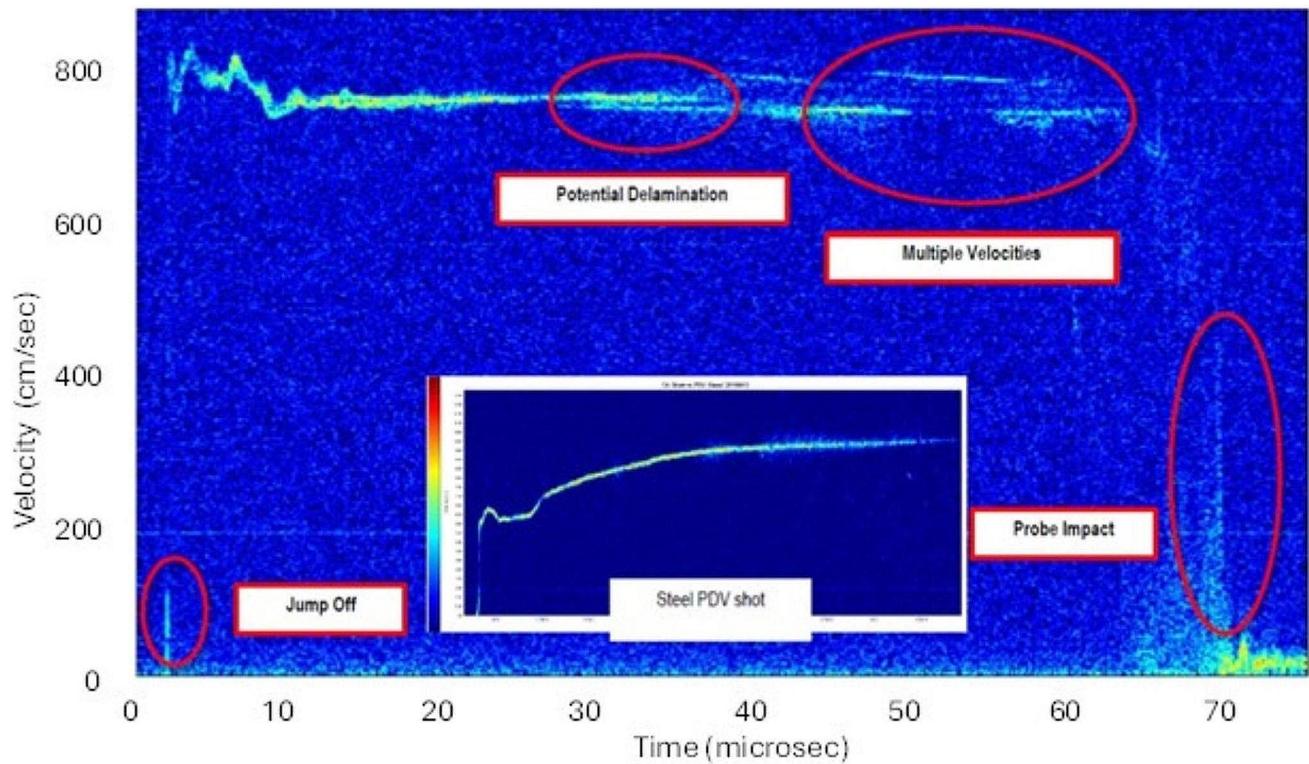


Fig. 7 Raw PDV trace of a CFC cylinder and PDV trace of a steel cylinder

moving rapidly, is intact when it is measured. The CFC data, however, shows only a brief period of a consistent and clear signal followed by what is a non-uniquely valued trace. This begins at around $35\mu s$ and becomes much more pronounced at approximately $45\mu s$. Behavior like this only occurs when the surface reflectivity has changed so much that a single strong signal no longer results. In this test, the leading edge of the material that the PDV laser is reflected from is intermingled with gaseous products, and/or is no longer a single reflective surface. All these factors are indicative of what would occur if the matrix had spalled or otherwise been broken into so many pieces that it no longer reflected the laser light as a single monolithic surface. An important aspect of this behavior is that after the point at which spall or fracture becomes apparent, the velocity data and everything derived from it can no longer be deemed accurate enough for use.

4 Explosive modeling

Modeling an exploding cylinder was undertaken using Abaqus and a multiscale technique that defines failure at the fiber and matrix material level. The rapid nature of detonation, occurring at the speed of 8193 m/s for Composition C4 at the density of 1602 kg/m^3 , meant that the problem needed to be treated explicitly, which is only conditionally

stable because explicit integration methods must take a time step lower than the Courant-Friedrichs-Lewy (CFL) condition. This requirement for stability states that the distance any information travels in each time step must be less than the distance equivalent to the elements of the finite element mesh. Ultimately this means that there are far more stringent requirements placed on the mesh density, and conditional stability is equally as important as convergence.

As the region of interest in this problem is the CFC sleeve, there was no need to treat the explosive contained within or the air or void on the outside with equal fidelity. Furthermore, the rapid expansion of the explosive products means that at best, such a region could be treated in an Arbitrary Lagrangian Eulerian (ALE) manner. Here, the explosive was treated as an Eulerian material without any loss of accuracy occurring in the region of interest. An option in Abaqus called CEL for Coupled Eulerian Lagrangian analysis was used for the present type of analysis because the CFC tube was modeled as a Lagrangian solid with an Eulerian high explosive and air regions surrounding it.

The present problem was comprised of an Eulerian domain consisting of approximately 141,000 EC3D8R Eulerian elements and a Lagrangian CFC sleeve composed of about 3408 SC8R linear shell elements from the standard element library. Shell elements were used considering the relative thickness of the structure in the radial direction.

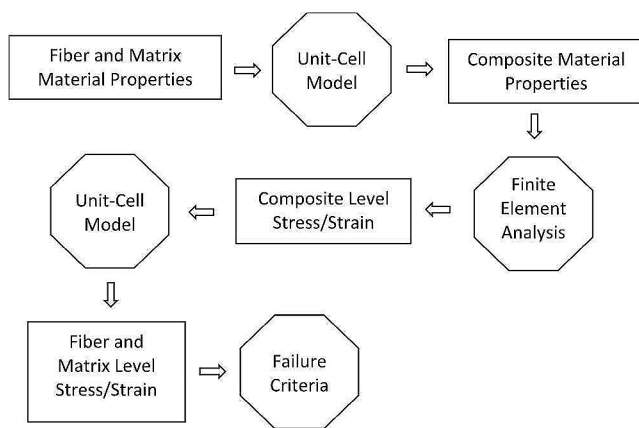


Fig. 8 Multiscale analysis

The high explosive was modeled using the Composition C4 JWL with explosive parameters given in Table 1. The only boundary conditions were applied to the exterior of the Eulerian region wherein no inflow was allowed but free outflow was permissible. At time 0 the high explosive, which had been shaped using the volume fraction option of the discrete field tool, was detonated and the detonation propagated downward from top to bottom just like in the previously described experiment.

A single shell element was used in the radial direction and the layer thicknesses and orientations were assigned under the section definition. The nodes corresponding to the precise locations at which the PDV probes were located during testing were included in the model. Then, the majority of the history output data was collected at the nodal points at a rate of one point every $0.1 \mu s$, and the computational model was run till $60 \mu s$ which was enough to investigate the transient motion and failure of the composite casing.

5 Multiscale modeling

Modeling the composite casing for a high-energy explosive was undertaken using Abaqus and a multiscale technique that defines failure at the fiber and matrix material level (Kwon and Darcy 2018a, b). The multiscale analysis links the behaviors of the fiber and matrix materials to that of the homogenized composite material. Figure 8 shows the schematic of the multiscale analysis.

The analysis starts with the fiber and matrix material properties, which are used to compute the effective material properties of the composite. To this end, the analytical unit-cell model is utilized. The computed composite material properties are then used for the finite element analysis. In this study, the transient structural analysis was conducted for the composite casing using the explicit time integration technique. The finite element analysis computes the

Table 2 Procedure of multiscale analysis

Step #1	Compute the effective material properties of the composite from the virgin properties of the fiber and matrix materials using the equations developed from the unit-cell model for the upscaling procedure
Step #2	Conduct finite element analyses of the composite structures using the effective material properties developed in the previous step
Step #3	Compute macro-level stresses and strains in the composite structures from the finite element analyses at the potential failure locations of the structures
Step #4	Decompose the macro-level stresses and strains into the micro-level stresses and strains using the equations developed from the unit-cell model for the downscaling procedure
Step #5	Apply the failure criteria to the micro-level stresses and strains to check for any potential failure
Step #6	If there is any failure in the fiber and/or matrix materials at any critical location, the properties of the corresponding material are degraded. Then, the degraded material properties are used to determine the updated effective material properties at the failed location. After that, repeat the computation from Step #2 above

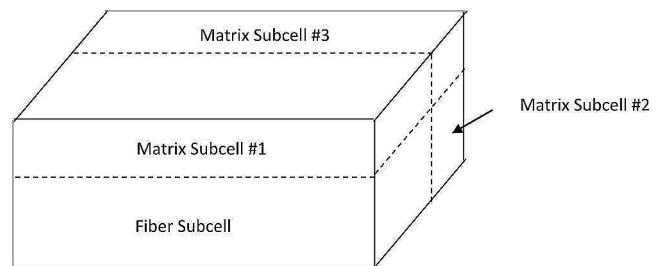


Fig. 9 Unit-cell model

deformation, stresses, and strains at the composite material level at every time step. These stresses and strains are again fed to the analytical unit-cell model to determine the stresses and strains at the fiber and matrix level. The former is called the macro-stresses and macro-strains while the latter is called the micro-stresses and micro-strains. Then, failure criteria are applied to the micro-stresses and/or micro-strains. This is a unique feature of the present multiscale analysis because almost every failure criterion is applied to the macro-stresses and/or macro-strains. Once there is a failure in any constituent material, its material properties are degraded, and a new analysis is conducted using the degraded material properties. Table 2 summarizes the procedure of multiscale numerical analysis.

The unit-cell model is sketched in Fig. 9. The unit-cell had four sub-cells considering two symmetric planes, one of which represents the fibers and the rest of them indicates the surrounding matrix material. For mathematical simplicity, the cross-sectional shape of every subcell is assumed to be square or rectangular. The fiber cross-section is considered to be square with a dimension equal to the square root of the

fiber volume fraction. Then, micro-stresses and strains are assumed uniform within every subcell but may vary among subcells to derive analytical solutions of the unit-cell model.

Every subcell has its constitutive equation depending on the fiber or matrix material. Stress equilibrium conditions are applied at the interface between any two neighboring subcells, and geometric compatibility conditions are also applied to the subcell strains. Furthermore, the unit-cell stresses and strains are considered volumetric averages of the subcell stresses and strains, respectively. The former is the macro-stress or macro-strain while the latter is the micro-stress or micro-strain. The details of the mathematical derivation are omitted here to save space, and they can be found in the references (Kwon and Darcy 2018a, b).

Once the micro-level stresses and strains are computed, failure criteria are applied to check any potential failure. There are three distinctive failure modes at the micro-level. They are fiber failure, matrix failure, and fiber-matrix interface failure. Therefore, there are three failure criteria.

The unified failure criterion was developed recently so that the criterion can be applied to a structural member regardless of the existence of a notch or not as well as the shape of the notch like a hole or a crack (Kwon 2021; Kwon et al. 2022; Kwon et al. 2024). The unified failure criterion is based on both stress and stress gradient conditions. For failure to occur, both conditions must be satisfied simultaneously. If only one of the conditions is satisfied, failure would not occur, yet.

The unified failure criterion is expressed as below:

$$\sigma_{eff} \geq \sigma_{fail} \quad (2)$$

$$\sigma_{eff} \geq \left(2E \left| \frac{d\sigma_{eff}}{ds} \right| \kappa_{fail} \right)^{1/3} \quad (3)$$

where σ_{eff} is the effective stress, σ_{fail} is the failure strength of the material, E is the modulus, and κ_{fail} is the second material property related to failure, which is similar to the critical energy release rate in fracture mechanics. Finally, s is the failure direction. Equation (2) states the stress condition while Eq. (3) states the stress gradient condition.

As the unified failure criterion is applied to the multi-scale analysis of fibrous composite structures, three failure modes at the micro-level have their own expressions for the effective stress. For the fiber failure, the effective stress is expressed as

$$\sigma_{eff}^f = \sqrt{\left(\sigma_x^f\right)^2 + \left(\frac{E_x^f}{G_{xy}^f}\right) \left[\left(\sigma_{xy}^f\right)^2 + \left(\sigma_{xz}^f\right)^2\right]} \quad (4)$$

where superscript ' f ' denotes the fiber, x is the fiber orientation, and E and G are elastic and shear moduli of the fiber material. Fiber failure could be tensile or compressive. In that case, the failure strength of the fiber σ_{fail}^f would be different depending on tension or compression.

The matrix material is considered an isotropic and homogenous material. In this case, the effective stress of the matrix is the maximum normal stress. Finally, the normalized effective stress for fiber-matrix interface failure is given below:

$$\frac{\sigma_{eff}^{int}}{\sigma_{fail}^{int}} = \left(\frac{\sigma_{xy}^m + \sqrt{v^f} (\sigma_y^m - \sigma_x^m)}{\tau_{fail}^{int}} \right)^2 + \left\langle \frac{\sigma_y^m}{\sigma_{fail}^{int}} \right\rangle^2 \quad (5)$$

Here, superscript ' int ' indicates the interface of the fiber and matrix, and v^f denotes the fiber volume fraction.

6 Numerical results and discussion

An early comparison of the model with an experimental image reveals reasonable physical agreement with experimental data as shown in Fig. 10. There are a few distinct differences between the experiment and numerical analyses, some of which are not the result of experimental variation. The largest difference resulted from an inability to synchronize the camera images to the recorded time due to variations in the Xenon flash bulb illumination time and duration. These bulbs were used for ad hoc illumination and are not precision items. Hence, although they were effective, their performance was not ideal. In addition, the RP-502 EBW used to initiate the detonation also has a half microsecond of function time deviation, which contributes slightly to some of the observed differences. In general, however, the surface of the model is a clear and distinct leading edge without any evidence of gaseous products leaking through a locally and irregularly damaged surface.

The wall velocity data is easily gathered from the numerical analysis and compared to the actual PDV data shown in Fig. 11. The increase in the initial wall velocity predicted by the numerical model closely matches that of the experimental data. This is before failure at the locations measured by the PDV. Final failure occurs as the solid explosive is converted to high-pressure gas which destructively expands the CFC cylinder. For metals like steel, anecdotal evidence suggested that this occurred around 3 volume expansions, but failure was expected sooner for a more brittle sample like CFC. Precisely when the failure occurs in time, however, remains to be determined later.

A noteworthy feature in the PDV data in Fig. 11 is an immediate jump followed by a subsequent decrease in

Fig. 10 Abaqus and experimental CFC wall at approximately $15 \mu\text{s}$

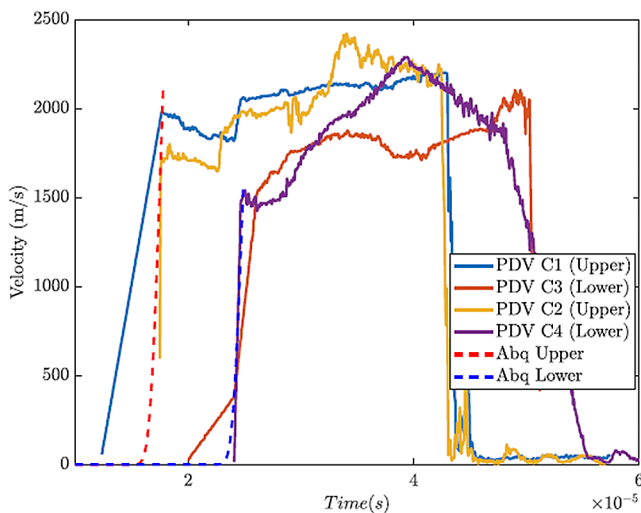
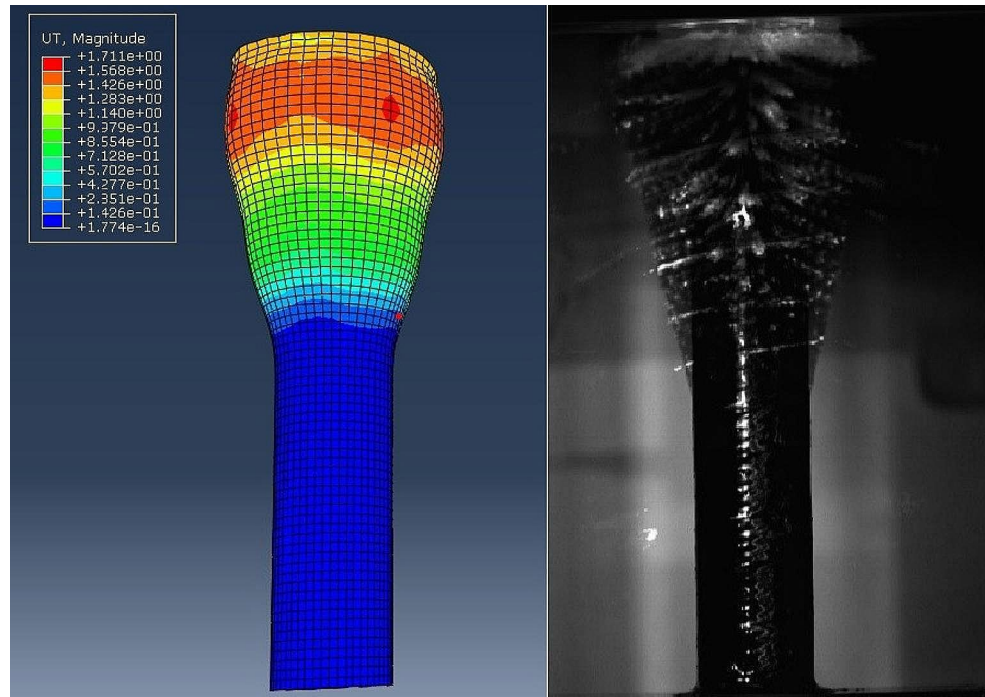


Fig. 11 PDV and Abaqus generated velocities

velocity that drops to a local minimum before again increasing rapidly. This local minimum, pronounced in all of the signals but channel 3, occurred at $4.9 \mu\text{s}$ and $6.4 \mu\text{s}$ after the initial peak at the upper PDV location while it occurred at $0.5 \mu\text{s}$ and $3.2 \mu\text{s}$ after the initial peak at the lower PDV location because two PDV were applied to the same location on the opposite sides. For the upper PDV location, this occurred between $22.6 \mu\text{s}$ and $24.1 \mu\text{s}$, and for the lower PDV site, this occurred between $28.0 \mu\text{s}$ and $28.7 \mu\text{s}$.

The immediate jump followed by the initial decrease in the velocity plot measured by the PDVs is considered as resulting from the failure of the CFC cylinder casing at the locations. As pieces are separated from the failing cylinders,

they are no longer constrained by the cylinder and move at higher velocities. As a result, the initiation of the failure at the locations would be the beginning of the immediate acceleration in the velocity plots, as discussed in the last paragraph.

To compare the failure time from the experiment to the numerical prediction, we adjusted the start time of the experimental data to be the same as that of the numerical model considering a small delay in the experimental data. Then, the time of the failure point of the CFC cylinder was $23.5 \mu\text{s}$ and $28.4 \mu\text{s}$, respectively, for the upper and lower sites of PVD measurement.

Once we determined the failure times at the locations measured by the PDVs, the multiscale analysis was conducted to predict the failure times. As stated in the last section, the effective material properties of the lamina were computed from the upscaling process. Then, those effective material properties were used in the analysis using Abaqus which computed the stresses and strains at each lamina of the CFC cylinder. The stresses and strains at each lamina were decomposed into those at the fiber and matrix materials. Finally, the failure criteria were applied to the fiber and matrix level stresses and strains. The critical failure would be the fiber failure at the lamina where the fibers carried the most load.

The failure criteria require the strength of the fiber and matrix materials. Among them, the fiber strength is more important because the fibers are the major load-carrying material. Furthermore, it was necessary to check the failure strength of fibers for high strain rates as experienced in the

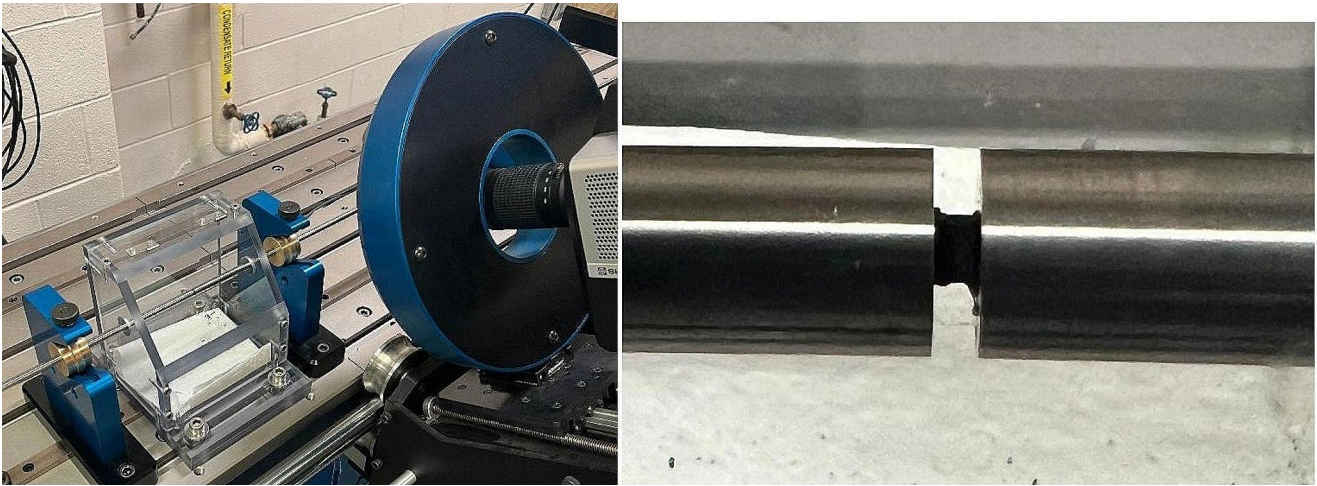


Fig. 12 SHPB setup (left) with closeup sample view (right)

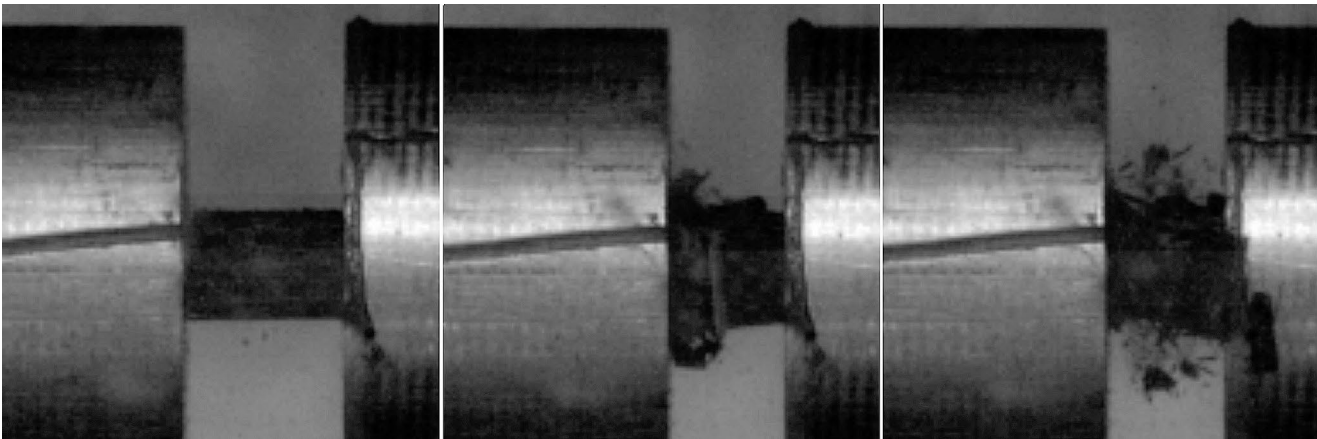


Fig. 13 CFC SHPB test snapshots at different time frames

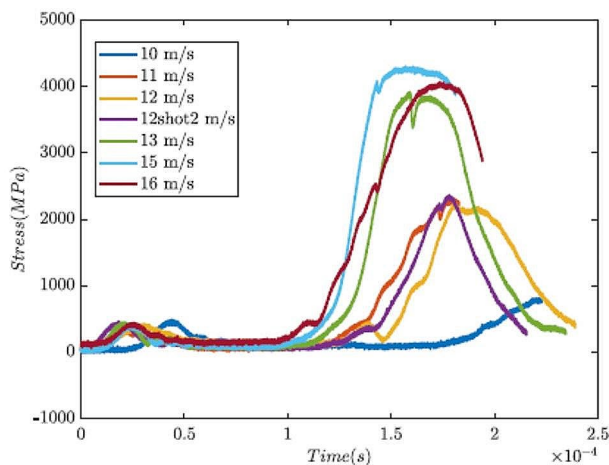


Fig. 14 CFC stress vs. time for 0-degree specimens for SHPB tests

present study because the strengths of most materials vary along with high strain rate loading. To determine the strength at high strain rates, Split Hopkinson Pressure Bar (SHPB) tests (Lindholm and Yeakley 1968; Gama et al. 2004; Gray & Blumenthal 2000) were conducted for the unidirectional CFC specimens. The specimen's size was 1 mm x 2 mm x 3 mm, where 3 mm was the direction for fiber orientation. Because we were interested in the fiber strength, A set of tests was undertaken such that the fiber direction was parallel to the axis of transmission of the shock loading for the SHPB setup. This was called 0-degree specimens. Figure 12 shows the test setup with a close-up view of a tested sample.

The SHPB testing resulted in the complete destruction of all CFC samples. Figure 13 shows a series of snapshots from a high-speed video taken at approximately 460k frames per second. The two plots of data that are of primary interest for this effort were the stress and strain rate as a function of time. The stress vs. time curve was used to bind failure from above. Seven specimens were conducted as 0-degree specimens. Figure 14 shows the stress time

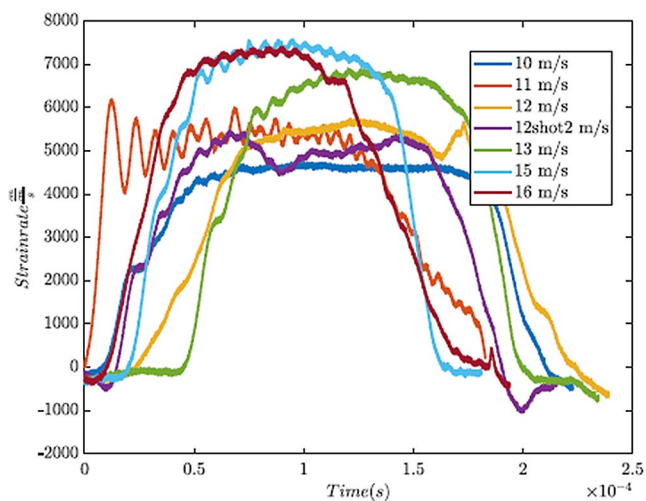


Fig. 15 CFC strain rate vs. time for 0-degree specimens for SHPB tests

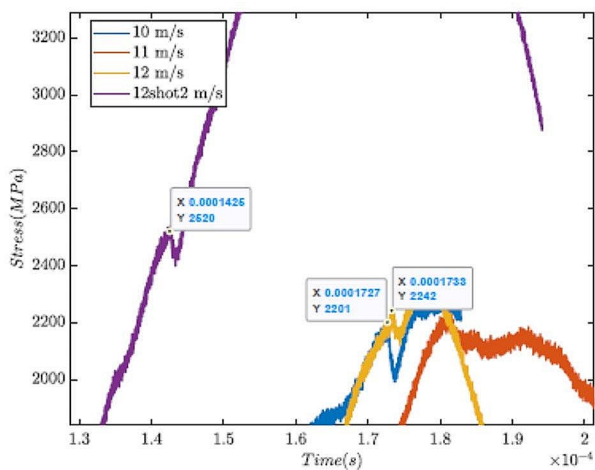


Fig. 16 Close-up of initial failure stresses in Fig. 14

history at different strain rates, and Fig. 15 shows the strain rate of the specimens. The strain rate plot suggested that the achieved strain rate from the SHPB tests was between $4,500$ and $7,500 \text{ s}^{-1}$. This strain rate was much lower than that experienced by the CFC cylinder casing containing a high-energy explosive as conducted in this study. However, the results from the SHPB tests were expected to suggest the effect of strain rate on the failure strength of the fibers, and the results were hoped to be extrapolated to determine the fiber failure strength at the strain rate of the present high explosive testing.

Because the SHPB tests were compressive, the specimens continued to support the load even after initial failure until the specimens turned into crumbles. This would not be the case if tensile loading were applied to the specimens. Thus, the initial failure strength was determined from the stress-time graph in Fig. 14, and that failure was the first peak stress followed by a drop in the stress plot. Figure 16

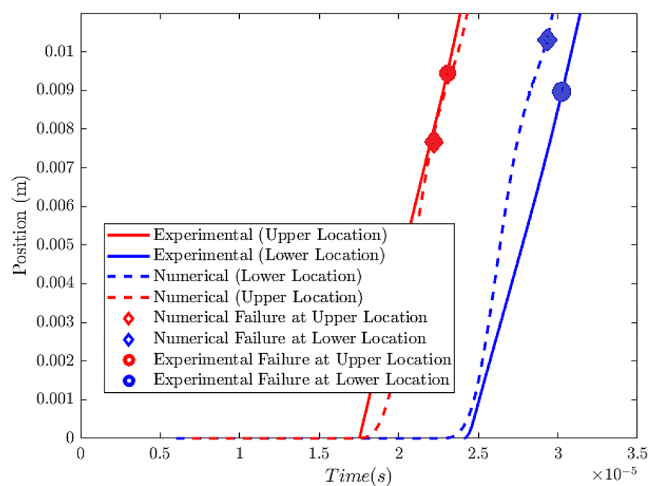


Fig. 17 Comparison of radial displacements between experiment and prediction

shows the close-up view of the initial failure stresses of the specimens.

Despite variation in strain rates, the mean stress for all the initial peak stresses was 2.32 GPa with a standard deviation of only 174 MPa . Such a small variation in the failure stresses suggests that the failure strength of the carbon fibers of CFC was nearly independent of strain rate because the fibers are the major load-carrying components along the 0-degree specimens. This result was also reported in previous studies (Zhou et al. 2007). Furthermore, this failure stress agreed well with the CFC composite with about 50% fiber volume fractions because the published strength of the present carbon fibers was around 4.5 GPa . Hence, the strain rate effect was not considered for the carbon fiber strength of the present composite cylinder.

Once the failure strength of the carbon fibers was determined to be rate insensitive, the prediction of the CFC cylinder subjected to internal high explosive loading was conducted. The radial displacements at the two PDV locations were plotted until the failure time in Fig. 17 to compare the prediction with the experimental results. Additionally, the hoop strains were also compared between the predicted failure and experimental observation in Fig. 18. The comparison shows a close agreement between the experimental and numerical results.

The numerical model assumed the nominal winding angles as inputted to the filament winding machine to fabricate the cylindrical composite casing. However, the actual winding angles may not be the same as the specified values. Such a difference in the winding angle can contribute to the error in the numerical predictions.

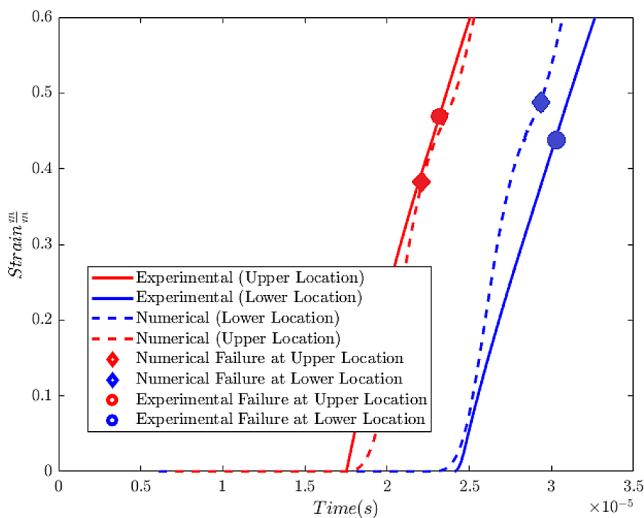


Fig. 18 Comparison of hoop strains between experiment and prediction

7 Summary and conclusions

Transient response and failure of a filament wound carbon fiber composite casing were investigated experimentally and numerically as the cylindrical composite casing was subjected to internal detonation of a high-energy explosive like C4. The detonation was initiated at the top plane of the composite cylinder and progressed downward. The high-energy explosive generated high pressure inside the composite cylinder resulting in very high strain rate deformation and subsequent failure of the cylinder. The whole explosion process occurred during about a couple of tens of microseconds. Unfortunately, strain gages did not work for this explosion testing as previously discussed. Instead, four PDVs were used to sense the radial deformations of the composite cylinder during the explosion process. A very high-speed video camera with 5 million frames per second was also used to capture the transient deformation and failure.

A multiscale and Multiphysics modeling and simulation was also conducted to supplement the experimental results. The Multiphysics part of the analysis was the structural analysis of the composite casing and the detonation of the explosive including surrounding air. The former was the Lagrangian model while the latter was the ALE model. The composite structure was modeled using a multiscale approach which computes micro-stresses at the fiber and matrix material level. Then, failure criteria were applied to the micro-stresses rather than macro-stresses.

Both experimental and numerical studies showed consistently the continuous growth of a cone shape of deformation of the composite cylinder as the detonation continued downward starting from the top. The PDV plots of the outer walls of the detonating CFC cylinder were quite different

from those of a similarly detonating metallic cylinder. The metallic casing showed a very distinctive line for the radial wall velocity during internal detonation because the metal stayed together under plastic deformation. On the other hand, the CFC casing showed much more noisy wall velocity plots because the material is brittle and there are multiple failure modes. The study indicated spalling of the matrix and separation of fibers without the bonding matrix, which eventually led to the failure of fibers into very tiny pieces. As a result, there were more scattered reflective lasers for the PDV probes.

The time of the major failure initiation was determined from the PDV plots, which showed a sudden increase in the velocity after an initial decrease. Such a sudden increase in the radial velocity was considered as the separation of the composite pieces, especially fibers, from the casing body. Numerical analysis was also used to predict the failure of fibers at the PDV-probed locations. The SHPB tests showed that the carbon fibers had material strength insensitive to the strain rates. As a result, the static strength of the carbon fibers was used in the failure prediction model based on the micro-stresses at the fiber and matrix material level. The failure prediction from the multiscale analysis agreed well with the experimental results in terms of both failure times and deformation up to failure.

The validated multiscale modeling technique will be useful for designing new composite casings for high-energy explosives while minimizing time-consuming and expensive repeated tests. Furthermore, the multiscale technique can be implemented in an optimization program for the optimal advanced design of composite casings for enhanced performance.

Acknowledgements This work was financially sponsored by the US Office of Naval Research.

Author contributions YW Kwon conceptualized, funded, directed, supervised, and wrote the paper. S DeFisher designed and conducted the experiment, performed the numerical study, and collected both experimental and numerical data.

Data availability The data will be available by request after completion of the project.

Declarations

Competing interests The authors declare no competing interests.

Conflict of interest The authors confirm there is no conflict of interest with this research.

References

- Alaei D, Kwon YW, Ramezani A (2019) Fluid-structure interaction on concentric composite cylinders containing fluids in the annulus. *Multiscale Multidisciplinary Model Exp Des* 2: 185–197
- Allison GE, Schriempf JT (1960) Explosively loaded metallic cylinders. II. *J Appl Phys* 31:846–851
- Ashkenazi E (1965) Problems of the anisotropy of strength. *Polym Mech* 1(2):60–70
- Beard AW, Palazotto AN (2006) Composite material for high-speed projectile outer casing. *AIAA Scitech Forum*, 6–10 January, AIAA 2020–0974.
- Blom AW, Stickler PB, Gürdal Z (2010) Optimization of a composite cylinder under bending by tailoring stiffness properties in circumferential direction. *Compos Part B: Eng* 41(2):157–165
- Daniel IM (2007) Failure of composite materials. *Strain* 43(1):4–12
- Dattelbaum D, Coe J (2016) The dynamic loading response of carbon-fiber-filled polymer composites. In: Silberschmidt V (ed) in *Dynamic deformation damage and fracture in Composite materials and structures*. Woodhead Publishing, Boston, MA, USA, pp 225–275
- Davies P, Choqueuse D, Bigourdan B, Chauchot P (2016) Composite cylinders for deep sea applications: an overview. *J Pressure Vessel Technol* 138(6): 060904
- Dolan D (2020) Extreme measurements with photonic doppler velocimetry (PDV). *Rev Sci Instrum* 91(5):051501
- Du N, Xiong W, Wang T, Zhang X-F, Chen H-H, Meng-ting Tan M-T (2021) Study on energy release characteristics of reactive material casings under explosive loading. *Def Technol* 17(5):1791–1803
- Franklin HG (1968) Classic theories of failure of anisotropic materials. *Fibre Sci Technol* 1(2):137–150
- Gama BA, Lopatnikov SL, Gillespie JW Jr (2004) Hopkinson Bar experimental technique: a critical review. *Appl Mech Rev* 57(4):223–250
- Gol'denblat I, Kopnov V (1965) Strength of glass-reinforced plastics in the complex stress state. *Polym Mech* 1(2):54–59
- Gray G III, Blumenthal WR (2000) Split-Hopkinson pressure bar testing of soft materials. *ASM Handb* 8:488–496
- Hashin Z (1980) Failure criteria for unidirectional fiber composites. *J Appl Mech* 47:329–334
- Hashin Z, Rotem A (1973) A fatigue failure criterion for fiber reinforced materials. *J Compos Mater* 7(4):448–464
- Hernández-Moreno H, Douchin B, Collombet F, Choqueuse D, Davies P (2008) Influence of winding pattern on the mechanical behavior of filament wound composite cylinders under external pressure. *Compos Sci Technol* 68:3–4
- Hinton M, Kaddour A, Soden P (2002) A comparison of the predictive capabilities of current failure theories for composite laminates, judged against experimental evidence. *Compos Sci Technol* 62(12):1725–1797
- Hur S-H, Son H-J, Kweon J-H, Choi J-H (2008) Postbuckling of composite cylinders under external hydrostatic pressure. *Compos Struct* 86:1–3
- Kaddour A, Hinton M, Smith P, Li S (2013) The background to the third worldwide failure exercise. *J Compos Mater* 47:20–21
- Kwon YW (2021) Revisiting failure of brittle materials. *J Press Vessel Technol* 143(6):064503
- Kwon YW, Darcy J (2018a) Failure criteria for fibrous composites based on multiscale modeling. *Multiscale Multidisciplinary Model Exp Des* 1(1): 3–17
- Kwon YW, Darcy J (2018b) Further discussion on newly developed failure criteria for fibrous composites. *Multiscale Multidisciplinary Model Exp Des* 1(4): 307–316
- Kwon YW, Sugimoto S (2020) Numerical study of implosion of shell structures. *Multiscale Multidisciplinary Model Exp Des* 3(4):313–336
- Kwon YW, Diaz-Colon C, Defisher S (2022) Failure criteria for brittle notched specimens. *J Press Vessel Technol* 144(5):051506
- Kwon YW, Markoff EK, DeFisher S (2024) Unified failure criterion based on stress and stress gradient conditions. *Materials* 17(3):569
- Lee E, Finger M, Collins W (1973) W JWL equation of state coefficients for high explosives, Lawrence Livermore National Lab. (LLNL), Livermore, CA (United States), Tech. Rep., 1973
- Lindholm U, Yeakley L L (1968) High strain-rate testing: tension and compression. *Exp Mech* 8(1):1–9
- Macapagal VP, Kwon YW, Didoszak JM (2024) Cylindrical single-wall and double-wall structures with or without internal water subjected to underwater shock loading. *Heliyon* e26930. <https://doi.org/10.1016/j.heliyon.2024.e26930>
- Mercier P, Benier J, Azzolina A, Lagrange J, Partouche D (2006) Photonic Doppler velocimetry in shock physics experiments. *Journal de Phys. IV (Proc.)* 134: 805–812
- Nelson SM, O'Toole BJ (2018) Computational analysis of blast loaded composite cylinders. *Int J Impact Eng* 119:26–39
- Noor AK, Burton WS, Peters JM (1991) Assessment of computational models for multilayered composite cylinders. *Int J Solids Struct* 27(10):1269–1286
- Puck A, Schürmann H (2004) Failure analysis of FRP laminates by means of physically based phenomenological models in failure criteria in fibre-reinforced-polymer composites. Elsevier, pp. 832–876
- Roy AK, Tsai SW (1988) Design of thick composite cylinders. *J Press Vessel Technol* 110(3):255–262
- Siromani D, Awerbuch J, Tan T-M (2014) Finite element modeling of the crushing behavior of thin-walled CFRP tubes under axial compression. *Compos Part B: Eng* 64:50–58
- Strand OT, Berzins LV, Goosman DR, Kuhlow WW, Sargis PD, Whitworth TL (2005) Velocimetry using heterodyne techniques. In: 26th international congress on high-speed photography and photonics, SPIE, vol. 5580, pp. 593–599
- Sun C, Quinn B, Tao J, Oplinger D (1996) Comparative evaluation of failure analysis methods for composite laminates, DOT/FAA/AR-95/109, Purdue University, School of Aeronautics and Astronautics, May
- Tan D, Sun C, Wang Y (2003) Acceleration and viscoplastic deformation of spherical and cylindrical casings under explosive loading. *Propellants Explosives Pyrotechnics* 28(1): 43–47
- Tennyson RC (1975) Buckling of laminated composite cylinders: a review. *Composites* 6(1): 17–24
- Tsai SW, Pagano NJ (1968) Invariant properties of composite materials. *Air Force Materials Lab Wright-Patterson AFB, Tech. Report*
- Tsai SW, Wu EM (1971) A general theory of strength for anisotropic materials. *J Compos Mater* 5(1):58–80
- Yao WJ, Wang XM, Li WB, Gu XH (2009) Effect of carbon fiber composite casing on blast power of explosive charge. *Adv Mater Res* 79–82: 461–464
- Zhou Y, Wang Y, Jeelani S, Xia Y (2007) Experimental study on tensile behavior of carbon fiber and carbon fiber reinforced aluminum at different strain rate. *Appl Compos Mater* 14:17–31